

Assessing the Detectability of Underground Water Pipe Leaks with Non-Invasive Technologies

Daniel Voysey

School of Surveying and Built Environment
University of Southern Queensland
danielvoysey@outlook.com

Glenn Campbell

School of Surveying and Built Environment
University of Southern Queensland
glenn.campbell@usq.edu.au

ABSTRACT

Underground water leaks cost Australian utility providers approximately \$840 million a year nationally in lost revenue. In this paper, the capabilities and limitations in applying Ground Penetrating Radar (GPR), infrared (IR) thermal and multispectral sensor Unmanned Aerial Vehicles (UAVs or drones) are determined by simulating underground water pipe leaks at varying depths (0.2 m, 0.3 m, 0.45 m). The presence of water manifested itself as an alteration to the soil's dielectric constant, resulting in a deepening of the pipe in comparison to the actual pipe depths on the GPR scans. This phenomenon was observed at all pipe depths from as early as one hour after beginning the leaks. The presence of water at the surface from the 0.2 m deep pipe leaks resulted in a decrease in surface temperature, allowing leak identification to occur from the thresholds determined. The IR thermal images were unable to identify leaks on the 0.3 m and 0.45 m deep pipes. Temperature-Vegetation Dryness Index (TVDI) images generated from the multispectral band images were inconclusive in identifying leaks. GPR and the 0.2 m deep pipe had the highest correctly identified leak detection rates. This research has generated a deeper understanding of employing these non-invasive technologies in leak detection, offering an efficient, low-cost option compared to current standard leak detection techniques.

KEYWORDS: *Ground Penetrating Radar, UAV, leak detection, non-invasive.*

1 INTRODUCTION

In Australia, it is estimated that on average 10% of all the water fed into the water networks by utility providers is lost due to leaks in the underground pipe networks (Water Services Association of Australia, 2020). With water being a finite resource in Australia due to drought conditions, the need to identify these leaks reliably and efficiently is a topic of interest to not only the utility providers but the country as a whole. It was estimated that water lost throughout the water distribution network cost the utility providers in the south-east Queensland region approximately \$117 million in the 2020-21 financial year (Australian Government, 2021). As the south-east Queensland region makes up only approximately 14% of the national population (Australian Bureau of Statistics, 2023), these figures equate to approximately \$840 million in revenue nationally lost to water leaks.

The main source of water that feeds these networks around the country are rivers and streams, which are mainly fed from rainfall. The Bureau of Meteorology is predicting reductions in

precipitation of between 1% and 8% for the south-east Queensland region (Australian Government, 2023), and this reduction in rainfall could lead to less water being input into the water networks, leading to water shortages, further increasing the need to reduce water losses.

Current practice to detect leaks is a combination of monitoring district areas during low times of usage (i.e. late night) with data loggers to identify potential leaks and then employing leak detection tools such as electro-acoustic devices and closed-circuit television to locate the leaks (De Coster et al., 2019). These processes can involve disruptions to the supply network, generating further costs for the utility providers, and generally require destructive techniques such as excavation to confirm the leaks once identified (Aslam et al., 2018). With the integration of infrared (IR) thermal cameras and multispectral (MS) sensors on Unmanned Aerial Vehicles (UAVs or drones) and the availability of smaller, easily portable and affordable Ground Penetrating Radar (GPR) units, these non-invasive technologies, not typically used in leak detection, could provide an efficient, low-cost option in identifying leaks in the underground water pipe networks.

1.1 Ground Penetrating Radar

GPR works by emitting electromagnetic pulses from a transmitter, which travel through the subsurface material with objects within the subsurface reflecting that signal back. The types of material that the emitted waves travel through will affect transmission velocity, with different materials having different dielectric constants (or relative permittivity) (Utsi, 2017). The presence of water within the subsurface should alter the relative permittivity of the soil, resulting in slower transmission speeds which will normally manifest as targets appearing deeper within the subsurface than expected. It is this phenomenon that is tested to detect water leaks in underground pipes.

The use of GPR to detect underground leaks has been widely researched with its use also being combined with other processes such as IR thermal imaging (Atef et al., 2016; Khader, 2016; Hawari et al., 2017) where GPR has been used to assist in determining the location of the underground pipe. Lai et al. (2016), Aslam et al. (2018), De Coster et al. (2019) and Aslam et al. (2022) all conducted experiments within a sand medium, while Cataldo et al. (2014) tested if different soil types had any effect on the detectability of the water leaks by conducting their experiment within a clayey soil and a silty soil. Cataldo et al. (2014) showed that soil type influenced the propagation speed of the emitted wavelength, affecting the radargrams produced. A variety of pipe materials has been tested, with Lai et al. (2016) and Aslam et al. (2022) both assessing the effect different materials have on the detectability of the water leaks. Metallic, polyvinyl chloride (PVC), polypropylene (PPR) and polyethylene (PE) have been covered between the two experiments, with the research showing that pipe material had little effect on the ability of GPR to detect the water leaks.

1.2 Infrared Thermal Imagery

Infrared thermal imaging is a process that captures the temperature of objects by detecting emitted radiation from the object in the IR range of the electromagnetic spectrum and converting this value to a temperature value using the Stefan-Boltzmann law (Thusyanthan et al., 2016). Depending on the time of year, weather conditions, soil type, pipe material and depth, the water within the pipe will generally be warmer or cooler than that of the surrounding material. As a leak occurs, the temperature of the waterlogged soil surrounding the pipe should

increase or decrease compared to the temperature of the dry soil (Shakmak and Al-Habaibeh, 2015), allowing these areas to be identified from the IR thermal images.

Infrared thermal imagery has been applied to the detection of underground leaks in a variety of simulated and existing conditions as a standalone process and coupled with GPR and MS imagery (Huang et al., 2010; Atef et al., 2016; Khader, 2016; Hawari et al., 2017). Atef et al. (2016), Khader (2016) and Hawari et al. (2017) all conducted controlled experiments testing what effects flying height and flying speed had on the ability of IR thermal imagery to detect underground leaks. Both Khader (2016) and Hawari et al. (2017) found that a camera height of 1 m and a flying speed of 2 km/h (0.28 m/s) was optimal for their experimental conditions, while the research conducted by Atef et al. (2016) concluded that a camera height of 2 m and a flying speed of 1.65 m/s was optimal. These differences are likely the result of variations in the surfaces and surrounding environments used within the respective experiments and are consistent with the findings of Hawari et al. (2017) who found that the three characteristics that impact the IR camera's ability to detect leaks are surface emissivity, surrounding environmental conditions (ambient temperature and relative humidity) and the operating conditions of the camera (flying height and flying speed). Emissivity is a ratio of a surface's ability to radiate energy at a temperature compared to that of a black surface (considered a perfect emitter) at the same temperature and will vary for different surfaces (Li et al., 2013).

Hawari et al. (2017) also found that slower flying speeds and lower heights were more suitable for surfaces with low emissivity and environments with low ambient temperatures and relative humidity. For high emissivity surfaces and high ambient temperatures and relative humidity, faster flying speeds helped to reduce noise due to the surrounding environmental conditions and the camera height having minimal effect on the results. This may explain the difference in operating conditions found by Atef et al. (2016) as the surface tested was a brick surface that has a high emissivity (Engineering ToolBox, 2003) and was conducted in high ambient temperatures (humidity was not noted).

1.3 Multispectral Imagery

Multispectral imaging is the process of collecting images in a combination of bands including visible, near infrared (NIR) and thermal infrared wavelengths and creating composite images from different combinations (Huang et al., 2021). Various indices generated from multispectral imagery have been used in leak detection. Initial research into leak detection concentrated on using the Normalised Difference Vegetation Index (NDVI) (Huang et al., 2010; Agapiou et al., 2016) and progressed to the Temperature-Vegetation Index (T-VI) (Chatelard et al., 2019; Krapez et al., 2020, 2022), which inspired the concept of employing the Temperature-Vegetation Dryness Index (TVDI) for leak detection (Sandholt et al., 2002; Chen et al., 2011).

Huang et al. (2010) used NDVI to identify potential areas of seepage or leaks within irrigation canals by visually assessing the images for areas with higher NDVI values compared to the surrounding areas as evidence of leaks present. They also found that NDVI was useful to eliminate false positives when used in combination with other sources such as thermal imagery where factors such as shadows can result in falsely identified areas. Agapiou et al. (2016) developed an automated process to assess NDVI images over an existing water pipe with a known leak site. By determining thresholds for the NDVI values from data taken with a spectroradiometer in the field, the NDVI images were assessed with any pixels within the determined thresholds identified as a potential leak site. NDVI images taken over a period of time were also assessed where any difference in NDVI values between images indicated an area

as a potential leak site. Both studies showed that NDVI can be successfully applied to leak detection in different situations with varying levels of success. However, their research indicates that this application is more suited to sites where the leak has been present for extended periods, allowing for the surrounding vegetation to grow and thrive on the water leaked from the pipe, returning higher greenness values.

T-VI, also referred to as the ‘triangle method’ named for the triangle-shaped scatterplot that is generated when a full range of varying soil moisture content and vegetation cover is represented in the dataset (Krapez et al., 2020), has been widely researched with similar methodologies to those employing NDVI utilised to identify leak locations. T-VI is computed using a combination of surface temperature determined from thermal imagery and a vegetation index (typically NDVI or Optimised Soil Adjusted Vegetation Index, OSAVI). Each pixel in the image is plotted with temperature as a function of a vegetation index to develop a scatterplot where pixels nearing the wet edge are thought to have higher moisture content compared to pixels near the dry edge (Chen et al., 2011). T-VI is applied to the detection of water leaks using the same principles as NDVI, where the presence of excess water from an underground leak has caused the surrounding vegetation to thrive, thus returning a stronger signal in the red and NIR bands when captured with a multispectral camera. The addition of the surface temperature component further improves the detectability of these wet areas by being able to differentiate between the ‘dry’ healthy vegetation areas and the ‘wet’ healthy vegetation areas.

Chatelard et al. (2019) and Krapez et al. (2020) employed the triangle method to identify potential leak sites with a Water Index (WI) over underground water pipes, with Chatelard et al. (2019) setting up an experiment over a simulated leak and Krapez et al. (2020) over an existing water pipe. Both experiments were able to positively identify (albeit not definitively) potential leak sites by analysing the generated WI images for areas with higher WI values. Both studies identified that while the experiments were able to identify the leak sites, factors such as shadows and the time of day/year that the images are captured influenced the ability to positively identify these potential leak sites since the Water Index is reliant on the surface temperature computed from the thermal imagery. Chatelard et al. (2019) concluded that the application of the WI should be carried out in the warmer months and long after any rain periods to maximise the surface reflectance and subsequent surface temperature used in calculating it.

Krapez et al. (2022) applied two versions of the triangle method (NDVI vs. IR and OSAVI vs. IR) across a wide range of conditions both on simulated and real-world leaks. They initially researched and tested many different multispectral images (single bands and combinations of bands) to assess the effectiveness in identifying leaks in water pipes and found that the T-VI combinations (as well as straight thermal IR images) produced the best results. Chatelard et al. (2019) and Krapez et al. (2020, 2022) showed that T-VI can also be successfully applied to leak detection, but their research showed that results can be greatly affected by factors such as weather and shadows with the level of success being related to the time of day and year that the images are generated. In optimal conditions, T-VI may be more suitable to identify shorter-term leaks as it is influenced by the surface temperature, which will fluctuate more rapidly due to the presence of excess water in the soil from the underground leaks.

The Temperature-Vegetation Dryness Index (TVDI) is a modified version of T-VI, which was further simplified by Sandholt et al. (2002) so that the wet edge is held parallel to NDVI on the x-axis and the dry edge is computed as a line fit to the data (Figure 1) with the dry edge given a value of 1 and the wet edge a value of 0. TVDI has typically been used as a means of assessing vegetation and soil water stress due to drought conditions (Rahimzadeh-Bajgirani et al., 2012).

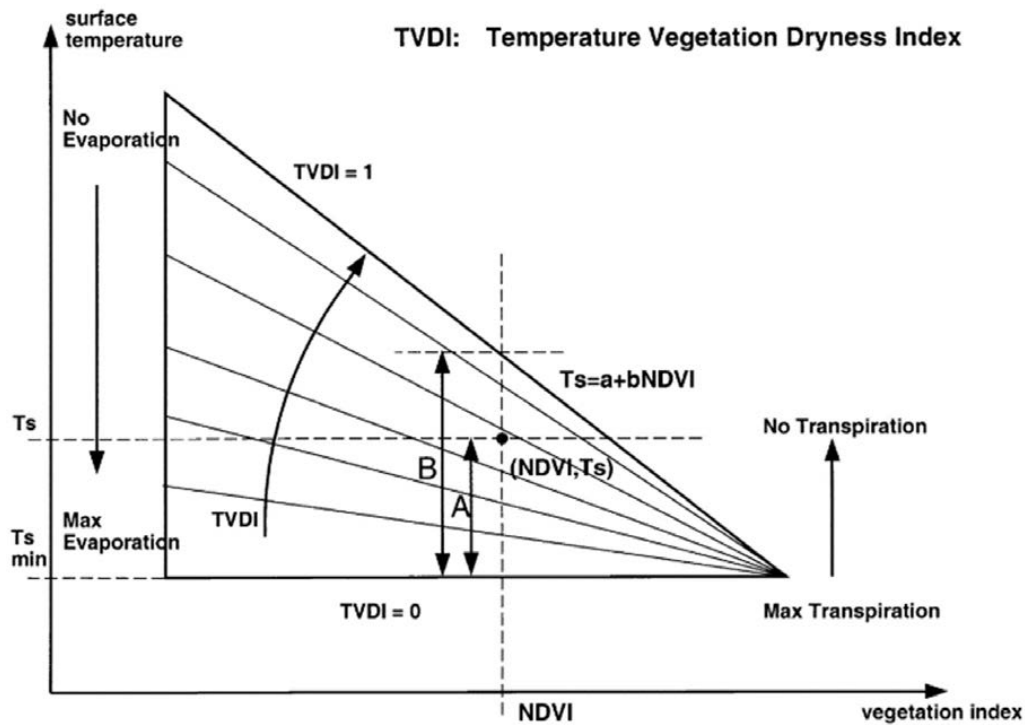


Figure 1: Graphical representation of TVDI. The triangle is turned on its side with NDVI held parallel to the x-axis and surface temperature on the y-axis (Sandholt et al., 2002).

Chen et al. (2011) applied a further modified TVDI in an experiment to determine the relationship between TVDI and soil moisture by statistically comparing TVDI values generated from multispectral satellite imagery against soil moisture values acquired from field studies. They applied a least-squares regression to statistically determine both the wet and dry edge, rather than holding the wet edge parallel to the x-axis. It was found that the TVDI values generated were a good indication of soil in the 10-20 cm depth range, but that TVDI poorly estimated soil moisture values in the 0-10 cm range. It was hypothesised that this poor correlation was due to multiple precipitation events over the test area during the experiment period, which caused high variations in the soil moisture values for that surface layer.

1.4 Remaining Challenges

Previous research has not undertaken direct comparison of all three non-invasive technologies, nor has the effect of varying pipe depths on the detectability of the water leaks been tested for any of the non-invasive technologies. This paper assesses both by testing the capabilities of the three non-invasive technologies against three varying pipe depths and comparing the results.

The majority of the GPR experiments reviewed were carried out within a controlled laboratory environment and tested on smaller pipe sizes not consistent with typical trunk infrastructure. It is possible to criticise the previous work for failing to use larger pipe sizes. The scope of this paper, however, does not permit this gap to be filled and restricts the experiment to pipe sizes consistent with previous research in order to allow a like-for-like comparison. The experiment presented in this paper was established outside of a controlled laboratory environment within the soil found on the chosen test site.

Previous studies (Atef et al., 2016; Khader, 2016; Hawari et al., 2017) have identified the optimal flying heights and speed for the use of thermal infrared cameras in leak detection, yet these flying heights (2 m above ground level) are not feasible in an urban environment due to

obstructions such as trees and buildings. This paper investigates if a flying height higher than that determined as optimal is still capable of identifying the underground water leaks.

The modified TVDI developed by Chen et al. (2011) has not been directly applied to the application of underground water pipe leak detection, yet the purpose of the index as a means of reporting on soil moisture or soil dryness could be applied as the index is generated from surface temperature, which will be affected by the presence of excess water due to the underground pipe leaks. It is theorised then that identified leak locations will have low TVDI values due to the presence of water from the underground leaks.

2 METHODOLOGY

This section outlines the non-invasive technologies employed, the test site chosen and the experimental setup, field processes and data processes used, and the data analysis undertaken to obtain the results.

2.1 Equipment

2.1.1 Ground Penetrating Radar

The Leica DS2000 ground penetrating radar has a dual-frequency antenna that emits signals on the 250 MHz and 700 MHz frequencies, allowing for low-resolution deep scans and high-resolution shallow scans simultaneously. It has a scan interval of 42 scans per metre of travel and when set to a sample rate of 512 will perform 381 scans per second per channel, of which the unit has two (Leica Geosystems, 2023). The GPR unit is set up and controlled by the uNext software, which shows live 2D radargrams of the deep and shallow channels (250 MHz and 700 MHz, respectively) as the unit travels forwards or backwards and saves the scans for post-processing.

2.1.2 Infrared Thermal Imagery

The DJI Mavic 2 Enterprise Advanced drone is equipped with a dual camera system, allowing simultaneous capture of visible and infrared thermal images. The thermal camera is capable of capturing images in the 8-14 μm spectral band range with a sensor resolution of 160 x 120 pixels (DJI, 2023a).

2.1.3 Multispectral Imagery

The DJI P4 Multispectral drone has six 1/2.9" CMOS sensors, one RGB for visible light images and five monochrome sensors for multispectral imaging. It is equipped with the following filters capturing the different spectral bands (DJI, 2023b):

- Blue (B): 450 nm \pm 16 nm
- Green (G): 560 nm \pm 16 nm
- Red (R): 650 nm \pm 16 nm
- Red Edge (RE): 730 nm \pm 16 nm
- Near-infrared (NIR): 840 nm \pm 26 nm

The P4 Multispectral drone has an integrated spectral sunlight sensor, capturing solar irradiance at the same time as image capture, allowing for more accurate post-processed data.

2.2 Experimental Site Location and Setup

The experimental site was located in the suburb of Camp Mountain, about 30 minutes west of the Brisbane CBD in south-east Queensland, Australia. It is a private property that covers 22,500 m², is generally flat and covered in grass with shrubs and medium to large trees. The predominant vegetation cover is short grass with small shrubs adjoining the area to the east and medium sized trees to the west. The experiment was conducted over an 11-day period at the end of July and start of August 2022. Typical weather for this time of year in the region is cool to mild, with dry days, cold nights and low levels of precipitation.

Three Ø 25 mm poly pipes were installed at depths of 0.2 m, 0.3 m and 0.45 m and a series of leaks simulated at different positions on each pipe. Figure 2 shows an overview of the experimental setup. Each pipe consisted of three simulated leaks and a control section at each end, which was left intact to assess the possibility of false positives. Each leak location and control section was then located by survey on the site datum to allow for leak identification processes to be performed in relation to the leak locations. The pipes were then buried, ensuring the soil was compacted back into the trenches with no voids within the soil present. The experimental rig was then connected to a 20,000 L water tank, which gravity-fed water into the system.

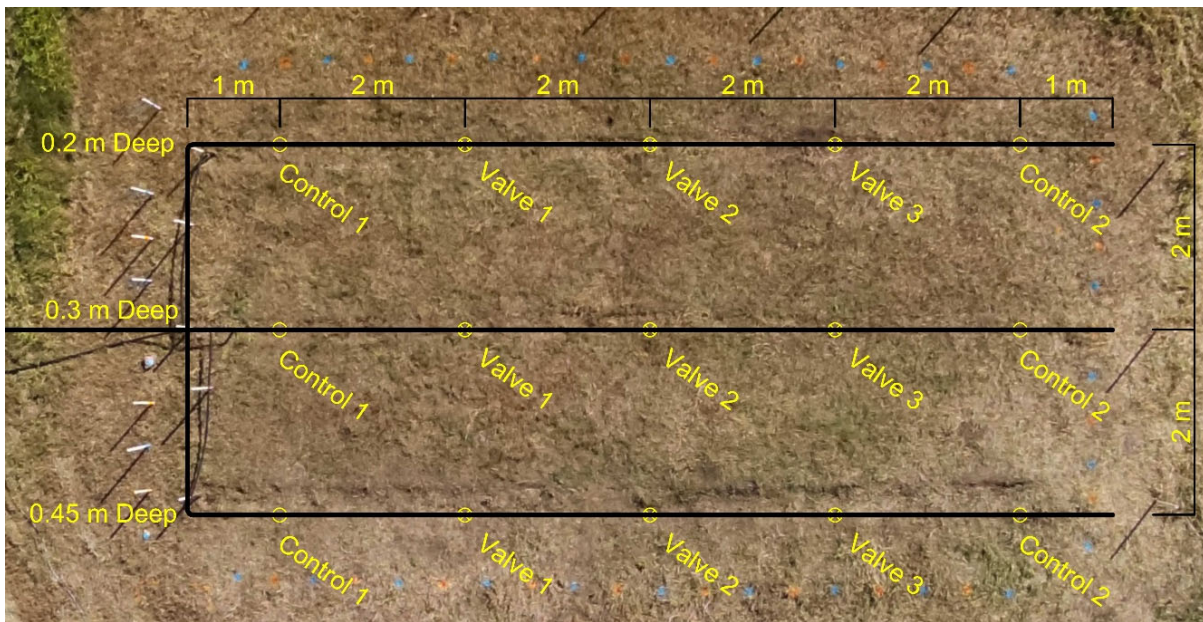


Figure 2: Overview of the experimental setup, showing the three pipes at varying depths and the locations of simulated leaks and control areas.

The valves used to simulate the leaks were set at a flow rate of approximately 2.0 L/hr, resulting in approximately 18.0 L of water leaked into the surrounding soil every hour. Scans with the GPR and images captured with the drones were then performed post start of the leak at 1 hour, 2 hours, 24 hours, 48 hours, 4 days, 7 days and finally 11 days. It is estimated that approximately 4,750 L was leaked into the surrounding soil during the 11-day testing period.

2.3 Field Processes

This section outlines the steps undertaken for each non-invasive technology to obtain the data for leak identification.

2.3.1 Ground Penetrating Radar

An equally spaced grid of 0.5 m aligned to each pipe and leak location was established over the buried pipes. The grid consisted of 19 scans performed perpendicular to the buried pipes and 11 scans parallel to the pipes. Perpendicular grids were aligned with the simulated leaks and the parallel grids to the buried pipes. Grids at either end of the pipes were chosen as the control sections where no leak was present.

The odometer of the GPR unit was calibrated over a known length prior to beginning the experiment and the self-calibration that is performed at the beginning of each set of scans conducted away from the buried pipes in the same location for each set of scans. A steady, consistent pace was then used to perform each scan.

2.3.2 Infrared Thermal Imagery

Ground Control Points (GCPs) were established around the experiment site on the site datum. For GCPs to be visible in thermal imagery, the target should have a differing emissivity value compared to the surrounding surfaces (Boesch, 2017). The experiment site was predominately grass and exposed soil, which have emissivity values of between 0.96-0.98 ϵ and 0.90-0.98 ϵ respectively (An et al., 2017). Aluminium foil was utilised on the GCPs, which has a low emissivity value. When paired with the dark carpet tile, the checkerboard pattern employed was also visible in the multispectral images.

Previous studies determined that flying heights between 1-2 m above ground level are optimal depending on certain factors (Atef et al., 2016; Khader, 2016; Hawari et al., 2017). However, this flying height is not feasible in most urban environments due to obstructions from structures such as buildings and trees. A flying height of 20 m was employed to assess if leak identification was still possible at higher flying heights.

The drone was manually positioned above the experiment site and overall images of the experiment site captured. Images were captured at mid-morning when the site was in full sunlight. Environmental site conditions such as ambient temperature, pressure and humidity were recorded at the time of flight for radiometric corrections performed in the post-processing software (Leblanc et al., 2021).

A section of the experiment site away from the buried pipes was saturated prior to flights being undertaken as a control area to determine the surface temperature values to be used in the leak identification process.

2.3.3 Temperature-Vegetation Dryness Index

The GCPs established for the thermal IR images were also utilised for the multispectral images taken to allow for image alignment during the data processing stage. The drone was manually positioned above the experiment site at a flying height of approximately 20 m and images captured of the entire site. The images were captured at mid-morning after capturing the IR thermal images. All six bands were captured but only the red and near-infrared bands were utilised in the data processing stage.

2.4 Data Processing

This section outlines the processing steps involved for each non-invasive technology to facilitate leak identification from the field data obtained.

2.4.1 Ground Penetrating Radar

The scan data was uploaded and processed in Geolitix, a cloud-based processing software. By performing the scans in a grid pattern, each scan can be positioned by inputting the project settings and profile parameters. For this project, equally spaced traces with a trace separation of 0.029 m and profile separations of 0.5 m were used. Since the deepest pipe depth was 0.45 m, the 700 MHz frequency was utilised because this allowed for higher resolution scans at the shallower depths.

The scan data was then cleaned by applying a time zero correction, an energy decay gain and a dewow and background subtraction filter. This step is vital in the leak identification process as the scan data is virtually unreadable without, as can be seen in Figure 3. Hyperbola fitting on a section of the pipe where no leak was present was then used to determine the signal velocity and dielectric constant of the soil.

The signal emitted from the GPR unit is shaped like a cone which spans a greater area as the signal travels deeper and is therefore projected out in front of the unit as it traverses forward. The signal is then reflected from the side of the pipe as the unit approaches with the shortest travel time (pipe depth) seen when the unit is located directly above the buried pipe and is then reflected off the side of the pipe again as the unit travels past the pipe, resulting in a hyperbola being formed (Utsi, 2017).

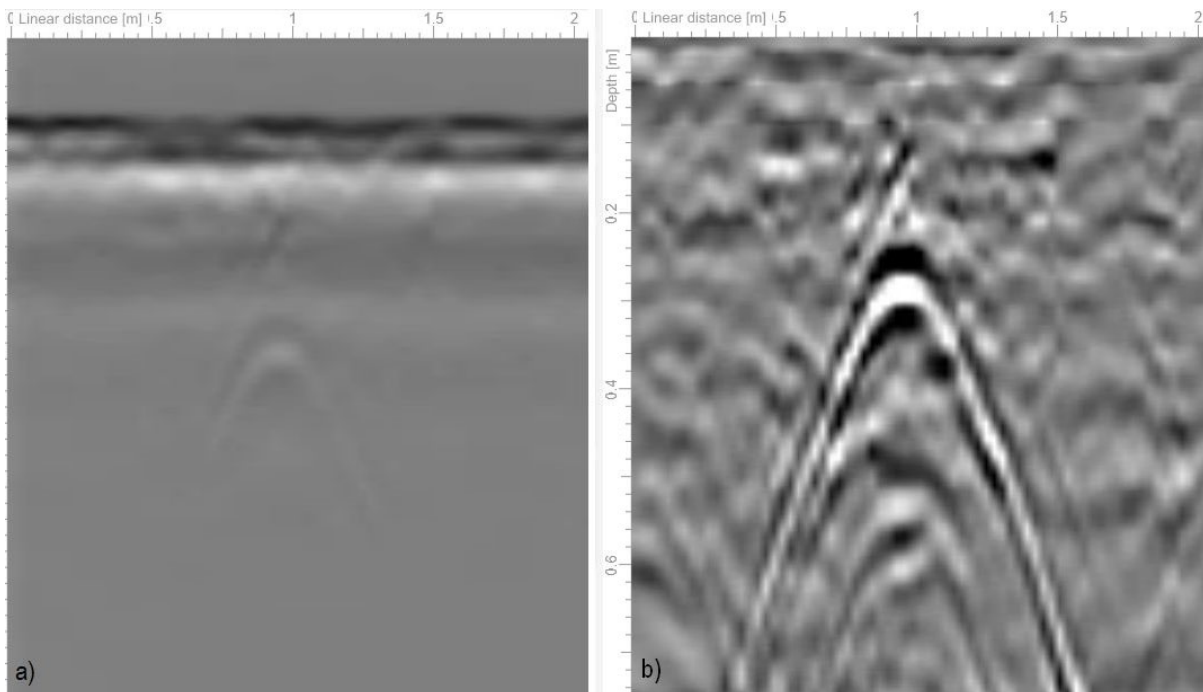


Figure 3: Scan data from the 1-hour post leak session (a) without the time zero correction, energy decay gain and dewow and background subtraction filters, and (b) with the correction, gain and filters applied. The hyperbola formed by the pipe can be clearly seen in the cleaned scan data.

The pipe depths were interpreted from the perpendicular scans by picking the apex of the hyperbola created from the buried pipe (see Figure 3b). For the longitudinal scans performed directly along the pipes, the pipe depth was determined via the automatic horizon algorithm within the software. If no definitive hyperbola was identifiable, then no interpretations were created for that scan at that pipe depth. The interpretations were exported to a spreadsheet with interpreted pipe depths plotted against travel distance.

The actual pipe depth and leak locations were plotted against the interpreted data. Leak identification was determined as an increase in pipe depth of 50 mm or more, that being twice the size of the pipe diameter, within the vicinity of the known leak locations. This identification was a combination of the perpendicular and longitudinal interpretations. Figure 4 shows the graph generated from the scan data for the 48 hours post leak session.

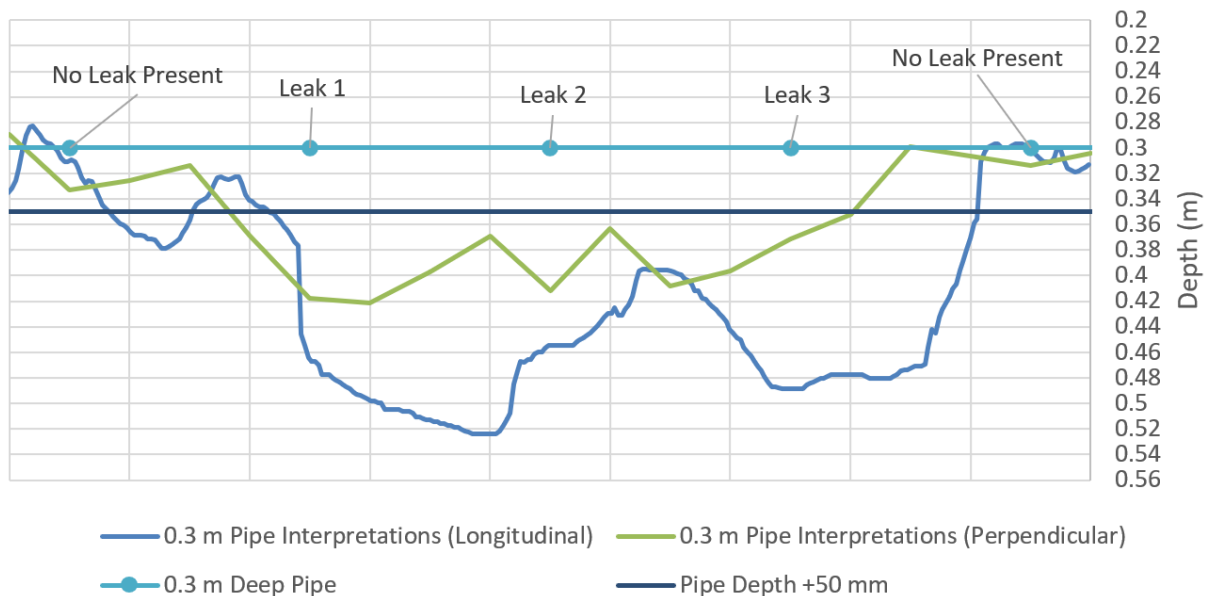


Figure 4: Interpreted pipe depths from the GPR scan data and the actual pipe with leak locations for the 0.3 m deep pipe after 48 hours. The increase in pipe depths at the leak locations can be seen due to the increase in soil moisture, decreasing the emitted wave velocity, resulting in a deeper than expected pipe.

2.4.2 Infrared Thermal Imagery

Images taken by the Mavic 2 Enterprise Advanced thermal camera, if not analysed within the native DJI software, do not contain any radiometric data for analysis within third-party programs. ThermoConverter by Aetha was used to convert the raw images to a JPEG file format with the radiometric data attached to each pixel within the image. The converted images were then imported into FLIR Tools, which allows for different surface temperature analyses to be performed (e.g. spot, line, polygon) and the application of highlighting areas based on thresholds.

The thermal images were captured during the mid-morning before the experiment site had been exposed to the sunlight all day, which resulted in potential leak sites, i.e. areas that experienced visible wetness within the soil, having surface temperatures lower than that of the surrounding areas. The average temperature and standard deviation for the experiment site were determined for each image from the radiometric values and thresholds set at between one standard deviation and three standard deviations below the average temperature, with those areas between the thresholds being highlighted. The images were then georeferenced over the experiment site and

1 m² identification boxes established over the known leak sites to facilitate leak identification. Each identification box was analysed, and if substantial areas of highlighting were present within the identification box, it was deemed that a leak had been identified.

2.4.3 Temperature-Vegetation Dryness Index

To generate the TVDI images, the thermal IR (used for surface temperature value T_m) and near-infrared (NIR) images were warped onto the red image pixel grid using a first-degree polynomial and nearest neighbour mapping algorithm. Once aligned, the NDVI vs. T_m scatterplots were generated, and lines of best fit determined visually for the dry and wet edges of the scatterplot. Figure 5 shows the generated scatter plot for the images captured on day 11 after the leaks were started.

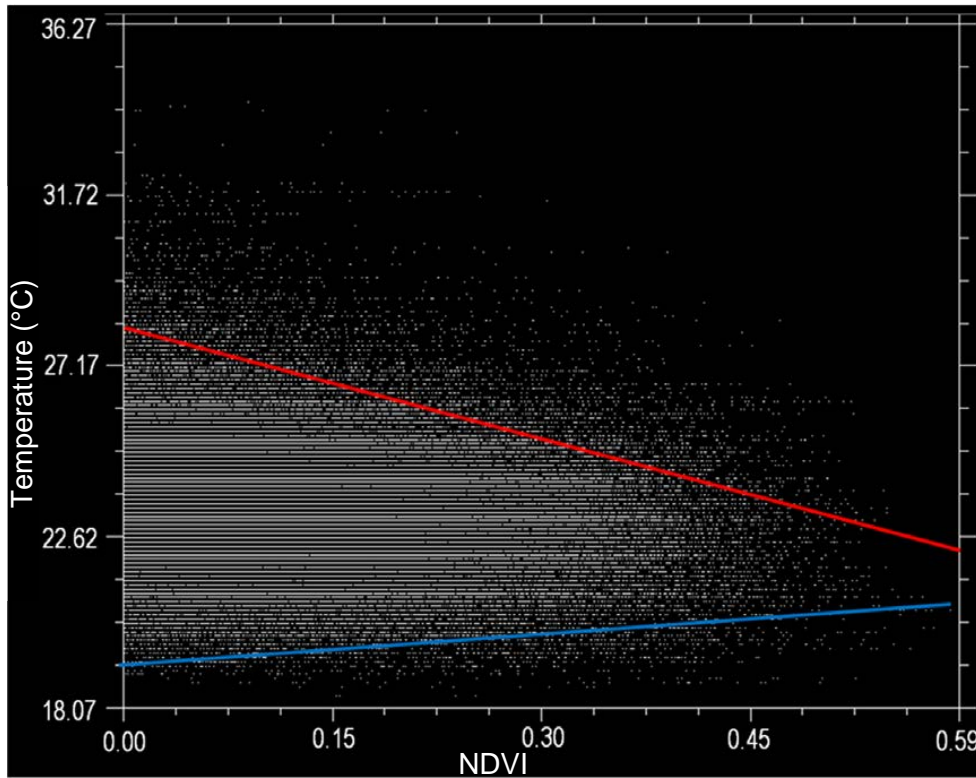


Figure 5: NDVI vs. measured surface temperature T_m scatterplot generated for the 11 days post leak session. The red line represents the dry edge and the blue line the wet edge. The parameters derived from each line are then used in Equation 1 to determine TVDI values.

The TVDI values were then calculated as follows (Sandholt et al., 2002):

$$TVDI = \frac{T_m - (a_w + b_w(NDVI))}{(a_d + b_d(NDVI)) - (a_w + b_w(NDVI))} \quad (1)$$

where T_m is measured surface temperature, a_d and a_w are the y-intercepts for the dry and wet edges and b_d and b_w are the slopes for the dry and wet edges, respectively.

The TVDI values for each pixel in the composite images were then calculated using the Raster Calculator in QGIS and images generated based on the TVDI pixel values. Finally, the images were assessed with the areas of low TVDI considered as potential leak sites.

2.5 Data Analysis

Confusion matrices were developed for each pipe depth and non-invasive technology for each session to determine the capabilities of each technology. A confusion matrix assesses each instance against one of four possible outcomes: true positive (TP), where a leak was present and accurately identified, false positive (FP), where a leak was not present but identified, true negative (TN), where no leak was present and none was identified, and false negative (FN), where a leak was present but not identified.

From the confusion matrix, the recall, accuracy and precision were calculated as follows to assess each technology's ability to accurately identify the leaks (Narkhede, 2018). F1-scores were then computed to compare the different pipe depths and non-invasive technologies (high F1-scores indicate better detection rates):

$$Recall = \frac{TP}{TP+FN} \quad (2)$$

$$Accuracy = \frac{TP+TN}{TP+FP+TN+FN} \quad (3)$$

$$Precision = \frac{TP}{TP+FP} \quad (4)$$

$$F1 - Score = \frac{2 * Recall * Precision}{Recall+Precision} \quad (5)$$

3 RESULTS AND DISCUSSION

3.1 Ground Penetrating Radar

The graphs generated from the GPR scan data interpretations consistently showed increases in the pipe depths where the simulated leaks were located, while the interpreted pipe depths were consistent with the actual pipe depths where no leak was present at either end of the pipe. Figure 1 shows a plot of the interpreted pipe depths for the perpendicular scans for the 0.2 m deep pipe over the course of the experiment. The perpendicular scan interpretations were given precedence over the longitudinal interpretations since the perpendicular interpretations were easily identified when hyperbolas were clearly defined in the scan data. The longitudinal interpretations were based on the in-built horizon fitting algorithm within Geolitix, and while the horizon was clearly identifiable in some instances (Figure 2), it was not as conclusive as the results from the perpendicular scans.

Similar results were obtained for the 0.3 m and 0.45 m deep pipes, with the interpreted pipe depths deeper than that of the actual pipe when in the vicinity of the simulated leaks. This phenomenon is seen due to the increase in soil moisture from the water leaks altering the dielectric constant of the surrounding soils. This in turn causes the emitted signal from the GPR unit to travel slower through the medium than expected, resulting in deeper interpretations for the pipe. This result is consistent with the findings of Cataldo et al. (2014) and Aslam et al. (2022).

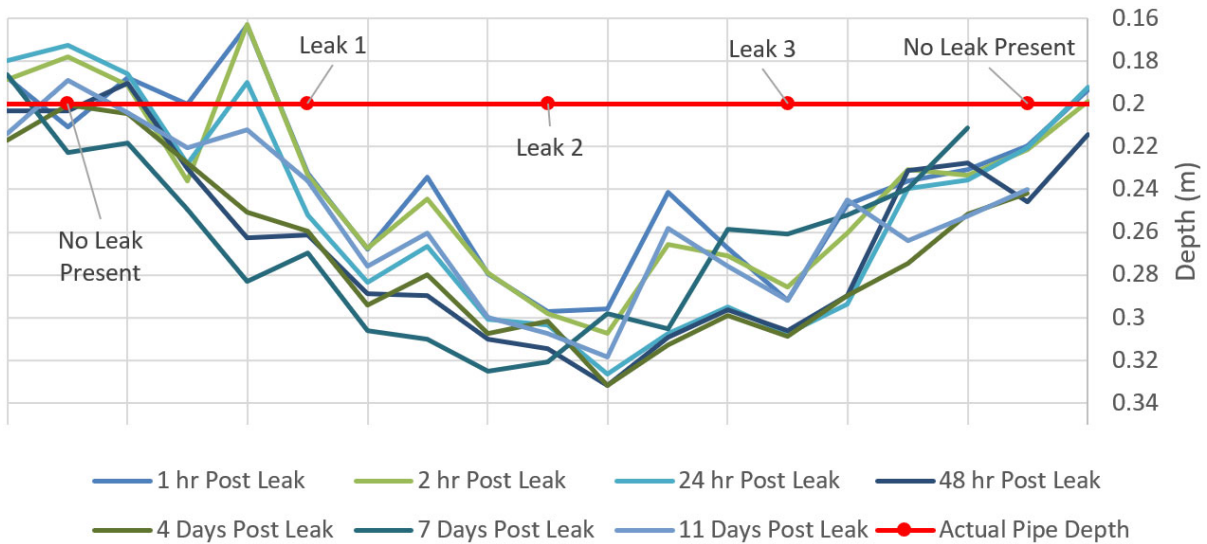


Figure 1: Combined pipe interpretations from the perpendicular scans for the 0.2 m deep pipe. The actual pipe depth and leak locations are indicated by the red line.

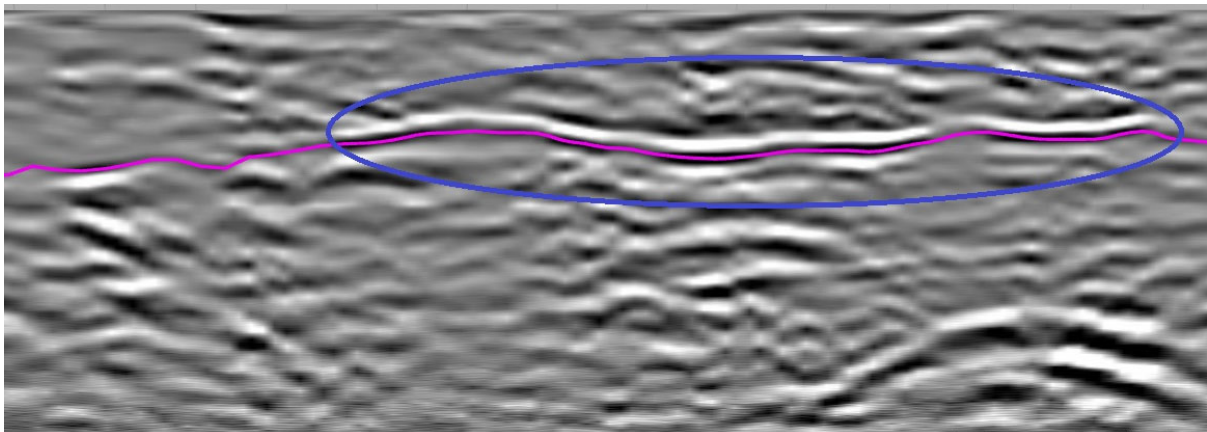


Figure 2: Pipe horizon interpretation from the longitudinal scan above the 0.3 m deep pipe during the 2 hours post leak session. The pink line represents the interpreted horizon. The blue ellipse indicates the section of pipe that has been clearly identified in the scan and which was used in determining the interpreted horizon.

As shown in Figure 1, while the interpreted pipe depths either side of the simulated leaks were higher than that of the location of the leaks in most cases, they were still not consistent with the actual pipe depths. This may be attributed to the water permeating horizontally through the trench between the leak locations due to the soil having been recently disturbed as well as vertically, causing a similar yet smaller alteration of the soil's dielectric constant to that observed at the leak locations. This indicates that the area affected by the leaks could be up to 4 m² (2 m by 2 m) surrounding the leak location. Further research with leaks spaced further apart may confirm the extent of the area of influence from the leaks.

Figure 3 shows the F1-scores for the GPR unit for each pipe depth during the experimental period. The GPR unit had a 100% accuracy and precision rate for all pipe depths for the sessions from 2 hours to 4 days post leak. The 0.2 m deep pipe had the best detection rate with an average F1-score of 0.95, compared to 0.86 for the 0.3 m deep pipe and 0.87 for the 0.45 m deep pipe. A decrease in F1-scores is visible over the last two sessions, with the scans performed 11 days after starting the leak having some of the lowest F1-scores for the entire period. The experiment site experienced small amounts of precipitation on days 5 and 10, which may have caused the decrease in detection rates due to increased amounts of moisture within the soil across the entire

site, not just localised to the leak sites.

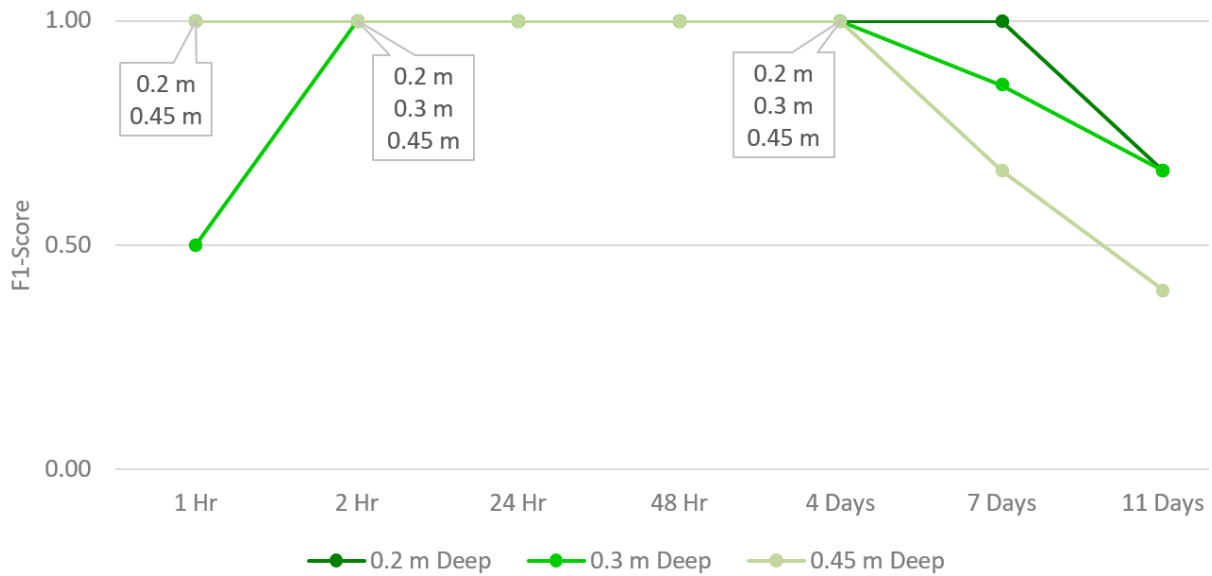


Figure 3: F1-scores for the GPR unit for each pipe depth in each session. The GPR was able to accurately identify the leaks with 100% accuracy and precision for the sessions between 2 hours and 4 days with a decrease in detection rates witnessed on the last day.

The 0.45 m deep pipe saw reductions in detection rates during the last two sessions with the 11 days post leak session receiving the lowest F1-score across all pipe depths for each session. The reduction in detection rates seen on day 11 may be attributed to the soil moisture content reaching a level that begins to deteriorate the emitted signal (Aslam et al., 2022). The deterioration of the emitted signal has more of a detrimental effect on the ability to detect the 0.45 m deep pipe in general as the signal is required to travel further than on the shallower pipe depths, resulting in lower detection rates.

A general rule of thumb when using GPR to detect pipes is that the maximum detectable depth for a pipe is between 5-10 times the pipe diameter (B. Keane, pers. comm.). Therefore, with the Ø 25 mm pipe, the maximum detectable depth is between 0.125 m and 0.25 m. This is not always the case as factors such as soil type, pipe material, antenna frequencies and signal scattering can affect the ability of the GPR unit in detecting underground pipes. Since the 0.45 m pipe was accurately identified in the scans for the first five sessions, the reduction in detection rates can be attributed to either the precipitation event or the soil moisture reaching a level that deteriorates the emitted signal due to the underground leaks. Further research employing larger pipes at greater depths would determine the maximum depth at which this non-invasive technology could detect the underground water pipe leaks.

The original experimental design was to continue testing the detection rates for a further 10 days (arriving at a total of 21 days) but was cut short due to the precipitation event. This extended period of testing, if the precipitation event had not occurred, would have determined if the leaks had caused the soil moisture to reach levels that began to deteriorate the emitted signal resulting in a reduction in leak detection rates. The precipitation event highlights a limitation in the use of this technology as the ability of the GPR to detect the leaks is dependent on the site having a certain level of 'dryness' to the soil, limiting the use to periods of no or low rainfall.

3.2 Infrared Thermal Images

During the experiment, visible wetness of the soil was observed on the 0.2 m deep pipe above valve 2. This area of wet soil was first observed during the 24 hour post leak session and was consistent throughout the experiment with signs of wet soil also observed above the other two leak locations on the 0.2 m deep pipe within 48 hours and the pipe trench eventually becoming entirely wet between the three leak locations and even spreading out past the trench to the sides by day 4.

Figure 4 shows the highlighted image generated from the 4 days post leak session. While the generated image has identified some areas as potential leak sites, the process has highlighted many other areas surrounding the test site where the grass was longer causing variations in the surface temperatures due to shading.

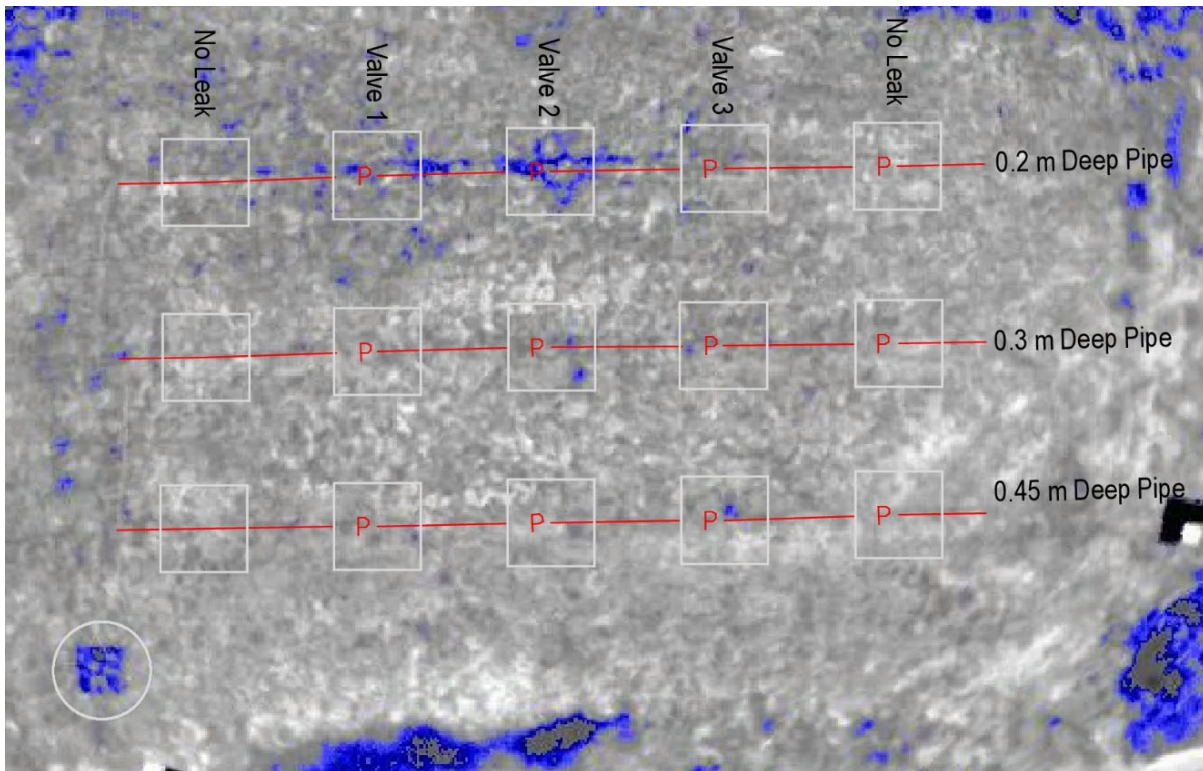


Figure 4: Highlighted infrared thermal image from the 4 days post leak session with the 1 m² identification boxes in white over the known leak locations. The areas of soil that were observed to be wet coincide with the highlighted areas over the 0.2 m deep pipe. The control wet section can also be seen in the bottom left of the image.

The images generated for the other sessions were consistent with that shown in Figure 4, with only the 0.2 m deep pipe leaks being consistently identified. Some instances of areas being highlighted as potential leak sites over the 0.3 m deep and 0.45 m deep pipe were observed in some images. However, no visible wetness of the soil was observed above either the 0.3 m or 0.45 m deep pipes. The principle, on which the leak detection with the IR thermal camera was based, was that the presence of water from the leak within the soil at the surface would increase or decrease the surface temperature. Since no visible wetness of the soil at the surface was witnessed, any leaks identified by the process above the 0.3 m and 0.45 m deep pipes could be attributed to variations in the surface materials, mainly that of bare soil, causing similar reductions in surface temperatures to those proposed to be caused by the leaks.

No leaks were identified during the 7 day post leak session for any of the pipe depths as the image was captured at the end of the day due to time-constraints as opposed to mid-morning. As an additional test, an increase in surface temperature instead of a decrease was used as threshold since the damp surface soil had experienced sun exposure all day and it was theorised that the surface temperatures would therefore be higher than the surrounding dry soil. No leaks were identified even though visible wetness above the 0.2 m deep pipe was observed on site. One factor that could affect the results seen for this session is that the experiment site was in full shadow by this time of day, which may have caused any variations in surface temperatures due to sun exposure to have evened out by the time the image was captured.

Figure 5 shows the F1-scores for the IR thermal drone for each pipe depth. The figure indicates that pipe depth has a significant effect on the ability of the IR thermal drone in detecting the underground pipe leaks as only leaks on the 0.2 m deep pipe were consistently identified. An increase in detection rates for all pipe depths was observed on the 11 days post leak session, which was attributed to the precipitation event experienced on site the previous day. The precipitation event increased the surface soil moisture on site, creating a similar effect to the surface temperatures as that experienced for the 0.2 m deep pipe due to the simulated leaks during the other sessions.

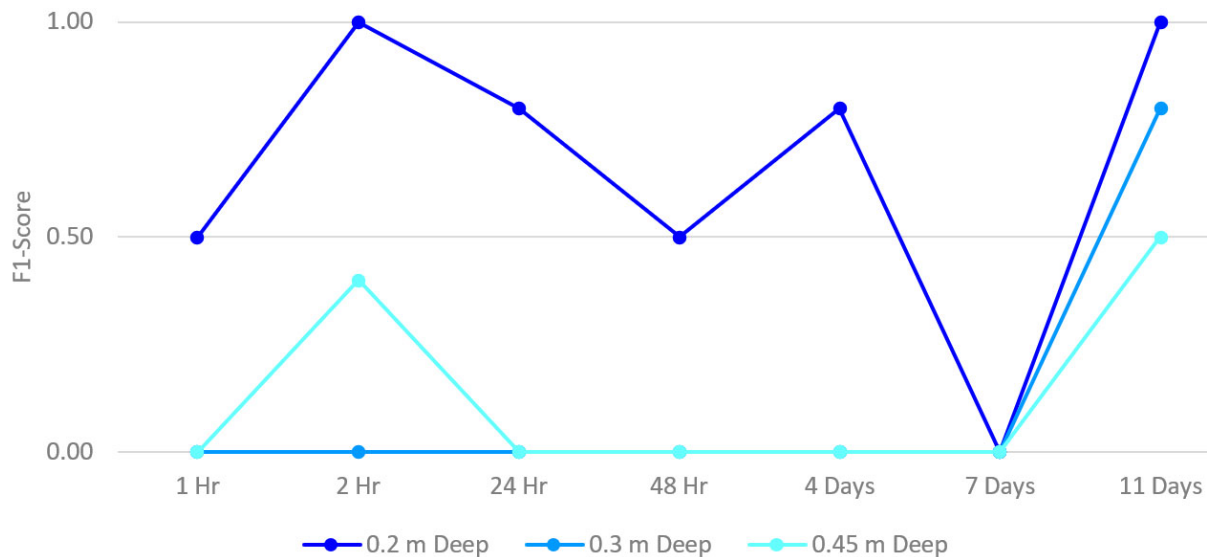


Figure 5: F1-scores for the IR thermal drone for each pipe depth in each session. The thermal images were only able to confidently identify leaks above the 0.2 m deep pipe due to the presence of visible dampness to the soil being observed. The increase in detection rates for all pipe depths on the last day were attributed to the precipitation event observed on site the day before.

A limitation in the use of this technology is that the time of day and year can affect the surrounding environmental conditions which affect the surface. The consequence of these factors is that no difference in surface temperature may be present, resulting in leak identification not being possible. The longer, unkempt grass surrounding the site and causing shading highlights a further limitation. Not all water pipelines are under well maintained areas, with many found under bitumen roads and concrete pathways instead of vegetated areas where this non-invasive technology and process would not be possible to employ for leak detection.

3.3 Temperature-Vegetation Dryness Index

The TVDI images generated were inconclusive and did not indicate any evidence of underground leaks. This inability to identify the leaks is attributed to the variations in surface

materials, being low grass or bare soil in this case, and the different optical properties these covers have, which was identified by Krapez et al. (2022) as the main cause of false alarms.

Figure 6 shows the generated TVDI image for the 11 days post leak session. The figure shows areas with low TVDI values above the 0.2 m deep pipe as well as some sections of the 0.3 m deep pipe. The control wet section can be seen clearly within the blue circle. The areas of low TVDI values are consistent with those areas where visible dampness of the soil was observed, which were highlighted in the thermal IR images, indicating that the surface temperature component of the equation is the determining factor in leak identification with this non-invasive technology.

Since the IR thermal image was used for the surface temperature component of Equation 1, and an increase in detection rates was observed for this session with the IR thermal images due to the precipitation event on the previous day, these results may be biased by that precipitation event. Potentially, for TVDI to accurately identify underground water leaks, a certain level of soil moisture is required. In this case, the precipitation event that occurred on the previous day appears to have provided this required increase, allowing for the leaks to be identified. However, this hypothesis will need to be tested with further works.

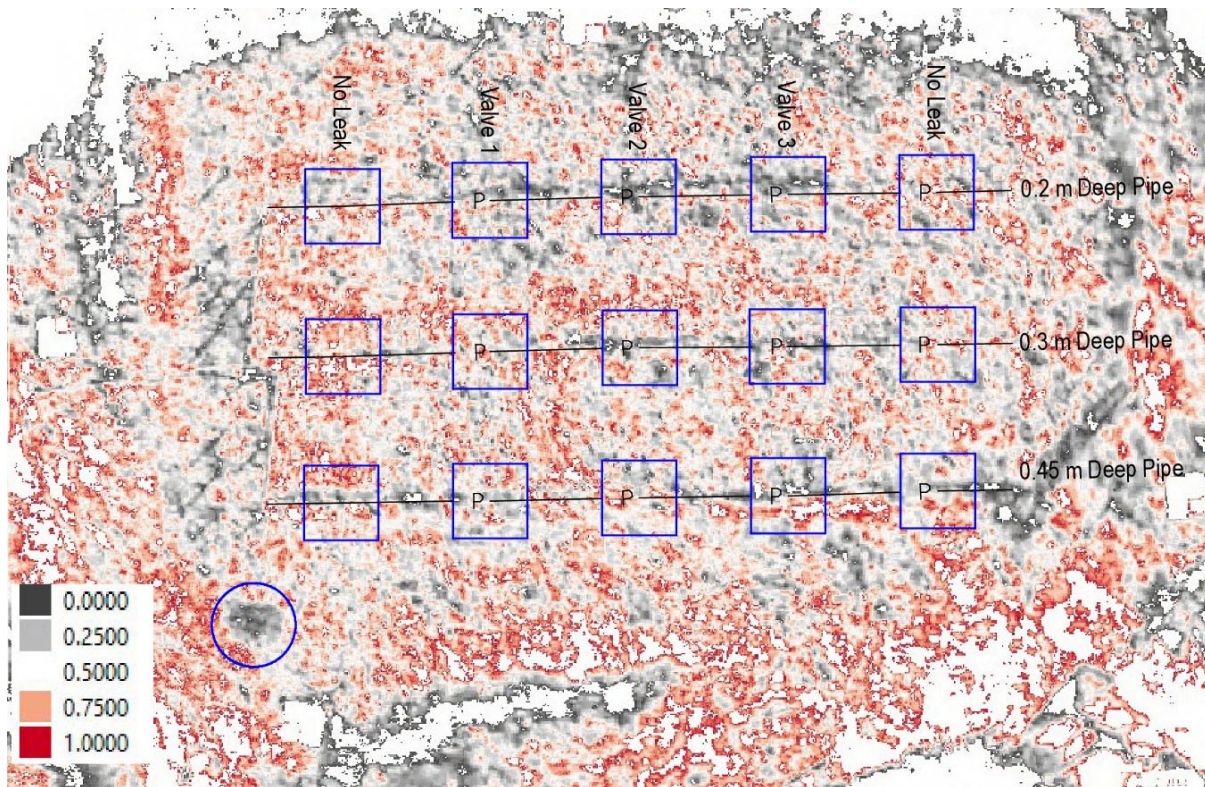


Figure 6: TVDI image generated for the 11 days post leak session. The light/dark grey areas indicate low TVDI values, being the areas with higher soil moisture. The area within the blue circle indicates the control wet section. Lower TVDI values above the 0.2 m deep pipe can be seen, which closely aligned with those areas highlighted in the thermal IR image.

The inability of the generated TVDI images to identify leaks may be attributed to the image's bandwidth captured by the drones being too broad. The thermal image band width on the Mavic 2 Enterprise Advanced drone is 6 μm . The P4 Multispectral drone red bandwidth is 32 nm and the NIR bandwidth is 52 nm. It can be assumed that a finer bandwidth, which is not achievable with the drones used, may be required for TVDI to identify the underground leaks. Further

research into bandwidths and TVDI’s response in those bands could fill this knowledge gap identified by this project.

Due to time constraints in the project, longer time periods were unable to be tested where it was theorised that the presence of the underground water leaks may influence the growth of the surrounding vegetation, as shown by Huang et al. (2010) and Agapiou et al. (2016), affecting the NDVI values used within Equation 1 and resulting in better detection rates.

3.4 Pipe Depth

The 0.2 m deep pipe had the highest detection rates of all three pipe depths with an average F1-score of 0.8 when the F1-scores for both non-invasive technologies were combined over the entire testing period. Figure 7 shows the average F1-scores for each pipe depth for each session during the testing period. It is evident that the 0.2 m deep pipe had the highest detection rates for every session while the 0.3 m and 0.45 m deep pipes both had similar detection rates. This indicates that pipe depth is a significant factor in leak identification regardless of the non-invasive technology employed.

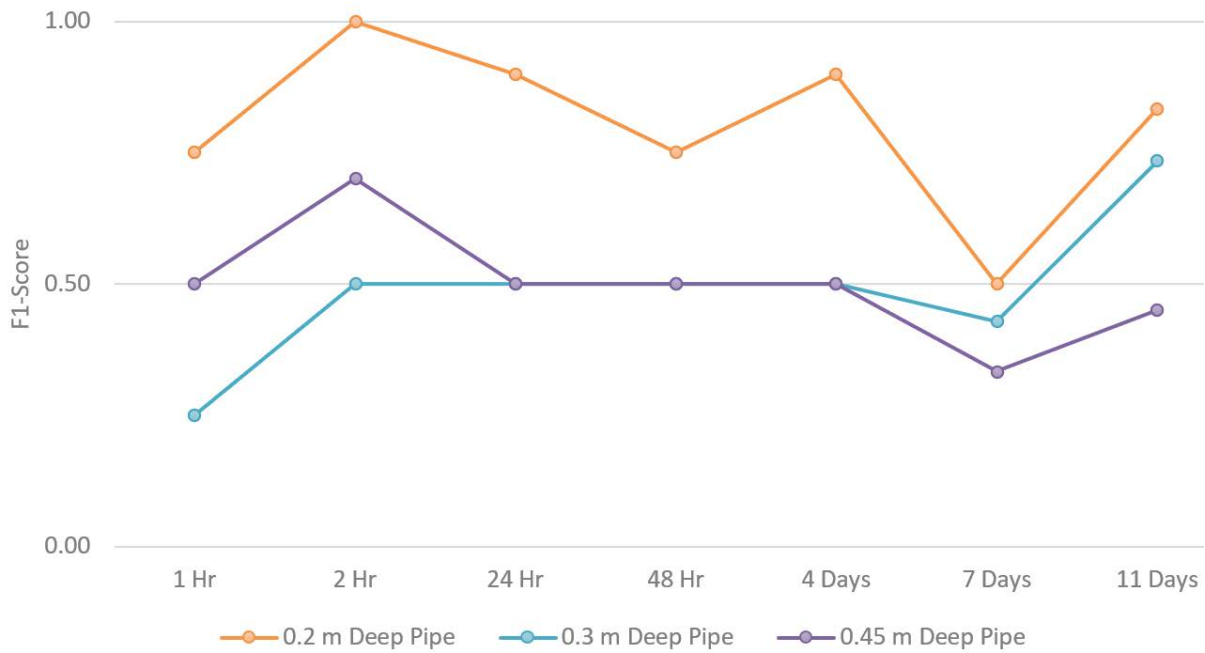


Figure 7: Average F1-scores for each pipe depth from a combination of both non-invasive technologies. The 0.2 m deep pipe had the highest detection rates for every session with the other two pipe depths having similar detection rates.

3.5 Overall Results

Table 1 shows the percentages for the correctly identified (true positive and true negative) and falsely identified (false positive and false negative) leaks for each technology over each pipe depth. The percentages were calculated from all seven sessions with each column having a sample size of 35 (21 simulated leaks and 14 control sections). It can be seen that the Ground Penetrating Radar was capable of accurately identifying the leaks on all three pipe depths at a rate of 86% for the 0.3 m and 0.45 m deep pipes and 94% for the 0.2 m deep pipe. Only the 0.2 m deep pipe for the infrared thermal images had an identification rate higher than 50% correctly identified, with a rate of 74%.

Table 1: Overall percentages of the correctly and falsely identified leaks for GPR and IR for each pipe depth. All three pipe depths with the GPR had higher correctly identified percentage rates than that of the 0.2 m deep IR rate, which had the best detection rates for that technology.

Pipe Depth	Non-Invasive Technology	Leak Identification (Overall)	
		Correct	Incorrect
0.2 m	IR Thermal	74%	26%
	GPR	94%	6%
0.3 m	IR Thermal	46%	54%
	GPR	86%	14%
0.45 m	IR Thermal	43%	57%
	GPR	86%	14%

These figures further confirm that pipe depth is the driving factor in leak identification with thermal IR whereas GPR is suitable for all three pipe depths.

4 CONCLUDING REMARKS

In this paper, three non-invasive technologies were tested to determine the capabilities and limitations in the detection of underground water pipe leaks. Each technology was tested on simulated leaks present on three pipes at varying depths over a period of 11 days. The results obtained indicate that the GPR unit is the most efficient in leak detection due to the presence of water from the leaks altering the soil's dielectric constant, resulting in the interpreted pipe depths from the scans appearing deeper than the actual pipe. This phenomenon was observed for each pipe depth and from as early as 1 hour after beginning the leaks. The ability of the IR thermal images to identify leaks was limited to those present on the 0.2 m deep pipe, indicating pipe depth to be a significant factor in leak detection with this non-invasive technology, while the TVDI images generated were inconclusive in identifying leaks.

This research has determined the capabilities and limitations of each non-invasive technology and has improved the understanding in employing these technologies in leak detection. Further research employing larger pipe sizes at greater depths with testing conducted over longer time periods will offer a deeper understanding of the potential of these non-invasive technologies in providing an efficient, low-cost option for identifying underground water pipe leaks.

ACKNOWLEDGEMENTS

This paper is based on the first author's undergraduate Honours research project at the University of Southern Queensland (USQ), which was awarded the APAS USQ Student Project Prize 2022. CadCon Surveying & Town Planning is acknowledged for making the GPR and equipment available for use, along with program licenses for ThermoConverter by Aetha and Geolix Cloud GPR Processing. The training and technical advice related to the GPR received from Brad Keane at CR Kennedy was much appreciated.

REFERENCES

Agapiou A., Alexakis D.D., Themistocleous K. and Hadjimitsis D.G. (2016) Water leakage detection using remote sensing, field spectroscopy and GIS in semiarid areas of Cyprus, *Urban Water Journal*, 13(3), 221-231.

- An N., Hemmati S. and Cui Y.-J. (2017) Assessment of the methods for determining net radiation on different time-scales of meteorological variables, *Journal of Rock Mechanics and Geotechnical Engineering*, 9(2), 239-246.
- Aslam H., Kaur M., Sasi S., Mortula M.M., Yehia S. and Ali T. (2018) Detection of leaks in water distribution system using non-destructive techniques, *IOP Conference Series: Earth and Environmental Science*, 150, 012004.
- Aslam H., Mortula M.M., Yehia S., Ali T. and Kaur M. (2022) Evaluation of the factors impacting the water pipe leak detection ability of GPR, infrared cameras, and spectrometers under controlled conditions, *Applied Sciences*, 12(3), 1683.
- Atef A., Zayed T., Hawari A., Khader M. and Moselhi O. (2016) Multi-tier method using infrared photography and GPR to detect and locate water leaks, *Automation in Construction*, 61, 162-170.
- Australian Bureau of Statistics (2023) Population, <https://www.abs.gov.au/statistics/people/population> (accessed Mar 2023).
- Australian Government (2021) National performance report 2020-21: Urban water utilities, Bureau of Meteorology, <http://www.bom.gov.au/water/npr/index.shtml> (accessed Mar 2023).
- Australian Government (2023) Australian water outlook – precipitation projections, Bureau of Meteorology, <https://awo.bom.gov.au/products/projection/precipitation/7.5.-27.133,152.838/nrm,-25.609,134.362/r/y/rcp45/2030> (accessed Mar 2023).
- Boesch R. (2017) Thermal remote sensing with UAV-based workflows, *The International Archives of Photogrammetry, Remote Sensing and Spatial Information Sciences*, XLII-2/W6, 41-46.
- Cataldo A., Persico R., Leucci G., De Benedetto E., Cannazza G., Matera L. and De Giorgi L. (2014) Time domain reflectometry, ground penetrating radar and electrical resistivity tomography: A comparative analysis of alternative approaches for leak detection in underground pipes, *NDT & E International*, 62,14-28.
- Chatelard C., Muñoz J.S., Krapez J.C., Mazel C., Olichon V., Polo J.B., Frédéric Y.M., Hélias F., Barillot P., Legoff I. and Serra G. (2019) Leak detection in water transmission systems by multispectral remote sensing with airplane and UAV, *Proceedings of IGARSS2019*, 7124-7127.
- Chen J., Wang C., Jiang H., Mao L. and Yu Z. (2011) Estimating soil moisture using temperature-vegetation dryness index (TVDI) in the Huang-huai-hai (HHH) plain, *International Journal of Remote Sensing*, 32(4), 1165-1177.
- De Coster A., Pérez Medina J.L., Nottebaere M., Alkhalifeh K., Neyt X., Vanderdonckt J. and Lambot S. (2019) Towards an improvement of GPR-based detection of pipes and leaks in water distribution networks, *Journal of Applied Geophysics*, 162, 138-151.
- DJI (2023a) Mavic 2 Enterprise series, https://www.dji.com/au/mavic-2-enterprise?site=brandsite&from=landing_page (accessed Mar 2023).
- DJI (2023b) P4 Multispectral, <https://www.dji.com/au/p4-multispectral> (accessed Mar 2023).
- Engineering ToolBox (2003) Emissivity coefficients common products, https://www.engineeringtoolbox.com/emissivity-coefficients-d_447.html (accessed Mar 2023).

- Hawari A., Khader M., Hirzallah W., Zayed T. and Moselhi O. (2017) Integrated sensing technologies for detection and location of leaks in water distribution networks, *Water Supply*, 17(6), 1589-1601.
- Huang S., Tang L., Hupy J.P., Wang Y. and Shao G. (2021) A commentary review on the use of normalized difference vegetation index (NDVI) in the era of popular remote sensing, *Journal of Forestry Research*, 32(1), 1-6.
- Huang Y., Fipps G., Maas S.J. and Fletcher R.S. (2010) Airborne remote sensing for detection of irrigation canal leakage, *Irrigation and Drainage*, 59(5), 524-534.
- Khader M.R.D. (2016) A non-destructive methodology for leak detection in water networks using infrared photography (IR) and ground penetrating radar (GPR), Masters thesis, Qatar University (Qatar), Ann Arbor.
- Krapez J.-C., Muñoz J.S., Chatelard C., Mazel C., Olichon V., Polo J.B., Frédéric Y.-M., Coiro E., Carreira D. and Carvalho A. (2020) Assessment of the triangle method (T-VI) for detection of water leaks from airplane and UAV, *Proceedings of IGARSS2020*, 4715-1718.
- Krapez J.-C., Muñoz J.S., Mazel C., Chatelard C., Déliot P., Frédéric Y.-M., Barillot P., Hélias F., Polo J.B., Olichon V., Serra G., Brignolles C., Carvalho A., Carreira D., Oliveira A., Alves E., Fortunato A.B., Azevedo A., Benetazzo P., Bertoni A. and Le Goff I. (2022) Multispectral optical remote sensing for water-leak detection, *Sensors*, 22(3), 1057.
- Lai W.W.L., Chang R.K.W., Sham J.F.C. and Pang K. (2016) Perturbation mapping of water leak in buried water pipes via laboratory validation experiments with high-frequency ground penetrating radar (GPR), *Tunnelling and Underground Space Technology*, 52, 157-167.
- Leblanc G., Kalacska M., Arroyo-Mora J.P., Lucanus O. and Todd A. (2021) A practical validation of uncooled thermal imagers for small RPAS, *Drones*, 5(4), 132.
- Leica Geosystems (2023) Leica DS2000 utility detection radar, <https://leica-geosystems.com/products/detection-systems/utility-detection-solutions/leica-ds2000-utility-detection-radar> (accessed Mar 2023).
- Li Z.-L., Wu H., Wang N., Qiu S., Sobrino J.A., Wan Z., Tang B.-H. and Yan G. (2013) Land surface emissivity retrieval from satellite data, *International Journal of Remote Sensing*, 34(9-10), 3084-3127.
- Narkhede S. (2018) Understanding confusion matrix, <https://towardsdatascience.com/understanding-confusion-matrix-a9ad42dcfd62> (accessed Mar 2023).
- Rahimzadeh-Bajgiran P., Omasa K. and Shimizu Y. (2012) Comparative evaluation of the vegetation dryness index (VDI), the temperature vegetation dryness index (TVDI) and the improved TVDI (iTVDI) for water stress detection in semi-arid regions of Iran, *ISPRS Journal of Photogrammetry and Remote Sensing*, 68, 1-12.
- Sandholt I., Rasmussen K. and Andersen J. (2002) A simple interpretation of the surface temperature/vegetation index space for assessment of surface moisture status, *Remote Sensing of Environment*, 79(2), 213-224.
- Shakmak B. and Al-Habaibeh A. (2015) Detection of water leakage in buried pipes using infrared technology; a comparative study of using high and low resolution infrared cameras for evaluating distant remote detection, *Proceedings of 2015 IEEE Jordan Conference on Applied Electrical Engineering and Computing Technologies (AEECT)*, 1-7.

Thusyanthan I., Blower T. and Cleverly W. (2016) Innovative uses of thermal imaging in civil engineering, *Civil Engineering*, 170(2), 81-87.

Utsi E.C. (2017) *Ground penetrating radar: Theory and practice*, Elsevier, Oxford, 206pp.

Water Services Association of Australia (2020) All options on the table: Urban water supply options for Australia, <https://www.wsaa.asn.au/publication/all-options-table-urban-water-supply-options-australia> (accessed Mar 2023).